Environmental Science & Technology

Article

Cite This: Environ. Sci. Technol. 2018, 52, 4546−4554

pubs.acs.org/est

In Situ Triaxial Testing To Determine Fracture Permeability and Aperture Distribution for CO_2 Sequestration in Svalbard, Norway

Jeroen F. Van Stappen,*[,∥,†] Redouane Meftah,[∥] Marijn A. Boone,[‡] Tom Bultreys,[∥,ϕ] Tim De Kock,[∥] Benjamin K. Blykers,[∥] Kim Senger,[§] Snorre Olaussen,[§] and Veerle Cnudde[∥]

[∥]UGCT-PProGRess, Department of Geology, Faculty of Sciences, Ghent University, Krijgslaan 281/S8, 9000 Ghent, Belgium

[‡]XRE NV, Bollebergen 2B bus 1, 9052 Ghent, Belgium

[§]Department of Arctic Geology, University Centre in Svalbard, P.O. Box 156, 9171 Longyearbyen, Norway

Supporting Information

ABSTRACT: On Svalbard, Arctic Norway, an unconventional siliciclastic reservoir, relying on (micro)fractures for enhanced fluid flow in a low-permeable system, is investigated as a potential CO_2 sequestration site. The fractures' properties at depth are, however, poorly understood. High resolution X-ray computed tomography (micro-CT) imaging allows one to visualize such geomaterials at reservoir conditions. We investigated reservoir samples from the De Geerdalen Formation on Svalbard to understand the influence of fracture closure on the reservoir fluid flow behavior. Small rock plugs were brought to reservoir conditions, while permeability was measured through them during micro-CT imaging. Local fracture apertures were quantified down to a few micrometers wide. The permeability measurements were complemented with fracture permeability simulations based on the obtained micro-CT images. The relationship between fracture permeability and the imposed confining pressure was determined and linked to the fracture apertures. The investigated fractures closed due to the increased confining pressure, with apertures reducing to approximately 40% of their original size as the confining pressure increased from 1 to 10 MPa. This coincides with a permeability drop of more than 90%. Despite their closure, fluid flow is still controlled by the fractures at pressure conditions similar to those at the proposed storage depth of 800−1000 m.

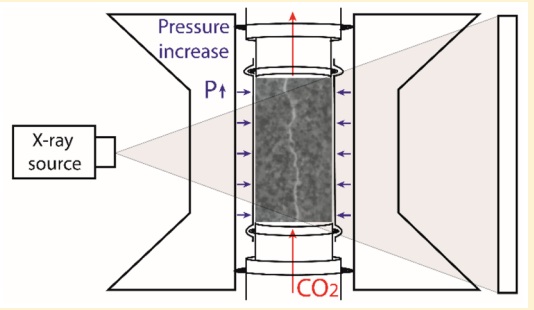

INTRODUCTION

The Intergovernmental Panel on Climate Change (IPCC) considers CO_2 capture and storage (CCS) projects as one of the options to reduce anthropogenic atmospheric CO_2 release.[1,2] From the 1970s onward, underground geological storage of CO_2 has been successfully explored both onshore and offshore.[3−7] Since 2007, the feasibility of a CCS project in Longyearbyen, Svalbard, has been under investigation,[8−10] with a ca. 300 m thick reservoir, comprising heterolithic sandstone-siltstone sections within the Upper Triassic De Geerdalen Formation, overlain by sandstones and thin conglomerates within the uppermost Triassic to Middle Jurassic rocks of the Wilhelmøya Subgroup (Figure S1c). These are considered unconventional because of their low to moderate matrix porosity and very low matrix permeability (<15% average porosity and a permeability $<1.0 \times 10^{-16}$ m^2 for the De Geerdalen Formation sections).[9,11,12] Successful water injection tests indicated that fracture permeability significantly affects fluid flow within these rocks[13] and positively impacts both injectivity and storage capacity.[9] This includes fracture-related secondary porosity and enhanced connectivity within the rock matrix due to microfractures.

Considerable effort has been directed to the structural characterization of the targeted sections in both outcrops and drill cores.[13,14] One of the most important properties of rock fractures is their aperture distribution, which directly affects the fluid flow and transport properties through them.[15] Fracture apertures in the reservoir sections were either determined indirectly, as hydraulic apertures from permeability measurements, assuming a single fracture with laminar flow,[16] or through high resolution X-ray computed tomography (micro-CT) imaging.[14] The latter allowed the direct measurement of fracture apertures in decompacted drill cores. Current advances in laboratory micro-CT, however, allow the direct investigation of the fracture apertures under triaxial pressure conditions.[17−21] Such advances include improved analysis tools for (micro)-fracture segmentation,[22−24] fracture aperture quantification,[25−27] and overall improved laboratory setups.[28−32]

In this study, naturally and artificially fractured rocks from the sandstone reservoir sections are subjected to confining pressures up to 15 MPa, in order to investigate the effect of burial depth on the fractures within them. These pressures mimic the effect of a burial depth of approximately 800−1000

Received: February 13, 2018
Revised: March 28, 2018
Accepted: March 29, 2018
Published: March 29, 2018

DOI: 10.1021/acs.est.8b00861
Environ. Sci. Technol. 2018, 52, 4546−4554

m on horizontal fractures within the rocks.[8,16] To investigate this, an experimental setup was constructed on a micro-CT system, allowing the study of rock plugs at reservoir conditions and visualizing the effect of stress on the fractures. Fracture apertures could be determined locally, with subresolution measurements on the micro-CT images. The micro-CT data also allows for fluid flow simulations through the rock fractures, adding to the understanding of the pore-scale transport. We thus provide the first direct information on fracture apertures at depth for the Svalbard storage unit. These experiments allow the interpretation of fracture measurements from decompacted core samples in order to understand their behavior at depth. The micro-CT images provide direct evidence of the dependency of the rock samples on the fractures for injectivity and storage of CO_2.

MATERIALS

The samples under investigation are part of the De Geerdalen Formation, which comprises fine to medium grained sandstones interbedded with silty shales and hard calcareous siltstones.[8,33] These rocks are exposed in both drill cores (depth 672−970 m at the planned injection site in Adventdalen) and nearby outcrops (Figure S1). In this study, a fractured sandstone interval from the outcrop at the southern shore of Isfjorden was targeted to determine the influence of microscopic fractures in these rocks. In a $6 \times 6 \times 6$ cm^3 sample, rock plugs parallel to bedding were prepared (5 mm diameter and 14 mm length) from areas where such horizontal fractures could be anticipated.[13,14] Experiments were performed on three individual rock plugs: one unfractured sample (INT-plug), one with a natural fracture parallel to the drilling direction (NF-plug), and one with an artificially induced fracture parallel to the plug axis (IF-plug). The artificial fracture was induced by a Brazilian test, in which the rock plug was subjected to diametrical loading to induce tensile stresses. All rock plugs are quartz-arenites, consisting of up to 70% quartz, less than 20% dolomitic cementation, and a limited amount of phyllosilicates (mainly muscovite and illite) filling the pores (<3%). Pyrite and plagioclase are also present to a lesser extent (<1%). Previous studies in similar rock material have combined information on fracture occurrences, aperture distributions, and fracture lengths in the outcrop materials with measurements in the drill cores.[13,14] The fractures in the rock outcrops might have undergone frost weathering, so that their length is larger than what is observed in the drill cores.[14,34]

METHODS

Permeability Measurements. A triaxial fluid flow setup was constructed, in which small-scale rock plugs were brought to reservoir conditions (Figure S2). In these experiments, no external temperature control was applied since the ambient temperature is similar to the actual reservoir temperature of approximately 30 °C at 700 m. The triaxial device, provided by SINTEF, Norway, allows one to impose fluid flow along the axis of the rock plugs. During the experiments, we measured the pressure difference (ΔP) between the inlet and outlet of the flow line. This allowed us to determine the permeability at a given confining pressure. According to Darcy's law, the sample permeability k (m^2) is

$$k = -\frac{\mu L Q}{A \Delta P} \quad (1)$$

with μ as the fluid's dynamic viscosity (Pa s), L as the length of the sample in the direction of the flow (m), Q as the volumetric flow rate (m^{3}s^{-1}), and A as the cross-sectional area of the sample (m^2).

For both the IF- and the NF-plug, the experimental approach is schematically represented in Figure S3. The IF-plug was first subjected to a stepwise increase in confining pressure up to 13.3 MPa. The axial pressure was kept constant at 5 MPa to ensure the stabilization of the investigated plug in the vertical direction. At each of the investigated confining pressures (1.3, 2, 4, 6, 8.2, 10, and 13.3 MPa), the IF-plug was saturated with a cesium chloride (CsCl) solution of 450 kppm and a micro-CT scan was taken. The CsCl-brine was chosen as a substitute for the formation water in the reservoir[35] and acts as a contrast agent for micro-CT scans. In spite of its salinity, the brine has a similar dynamic viscosity as H_2O.[35] Micro-CT scans were taken with the environmental micro-CT system (EMCT) at Ghent University.[27,36,37] The scanning parameters are given in Table T1. Because the IF-plug contains a well pronounced fracture, it was possible to easily switch pore fluids during the experiments. At each of the confining pressures, the brine in the fracture was therefore drained with CO_2, after which a second micro-CT scan was taken. During the CO_2 injection, radiographs were taken continuously to ensure that only the fracture inside the plug was drained and not the rock matrix. More information on the precise process of the CO_2 injection is available in the Supporting Information. By registering the CsCl-brine filled images to the fracture-drained images, differential images could be constructed to segment the fracture,[24] which allowed fluid flow simulations within the 3D volume of the fracture.

At the different confining pressures, the permeability was determined by imposing a constant brine or water flow rate, so that the pressure drop across the rock plug fluctuated around 0.5 MPa. This pressure drop was monitored for 15 min and averaged to determine the permeability at a given confining pressure. At higher confining pressures, a lower flow rate was used to achieve the pressure drop of 0.5 MPa. Calculation of the Reynolds number[38] showed that the flow rate was still well within the laminar regime ($Re < 8.5 \times 10^{-3}$ for all experiments). Therefore, the Darcy equation is still valid.

For the NF-plug, four different confining pressures (2.9, 5, 10, and 15 MPa) were chosen at which micro-CT scans were made with identical parameters as used in the scans of the IF-plug. Because of the low inherent permeability of the plug and fluid injection pressure limits, these first scans were carried out without pore fluids. Afterward, the confinement around the sample was brought back to atmospheric conditions, followed by a relaxation period of 72 h. The triaxial experiment was subsequently redone, now with a complete saturation of the pore space with the CsCl-brine, followed by a third time saturated with H_2O. The experimental determination of the permeability in function of the confining pressure was thus determined twice: once with the CsCl-brine (at confining pressures of 1.0, 2.8, 4.5, 5.1, 6.6, 8.0, and 10 MPa) and a second time with H_2O (at confining pressures of 1.0, 3.0, 4.0, 5.1, 6.4, 8.0, and 10.0 MPa). In this second and third run of the triaxial test, micro-CT scans were also taken at different confining pressures. However, differential images with the dry state could not be obtained, since the fracture remained partly closed after the first run of the experiment. The permeability of the INT-plug was determined at four different confining pressures (1.0, 2.1, 4.0, and 5.0 MPa), using the CsCl-brine. At higher confining pressures, the permeability of this plug could

DOI: 10.1021/acs.est.8b00861
Environ. Sci. Technol. 2018, 52, 4546−4554

no longer be determined due to pressure (max 0.68 MPa) and flow rate limitations (min 0.004 μL/s) in relation to the inherent low permeability of the plug.

Hydraulic Aperture Quantification. To obtain an indication of the fracture's aperture, the experimentally determined permeability of the rock plugs can be used. Through a simplification of the fracture within the rock plug to the parallel plate representation,[39] the fracture permeability k_f with laminar flow can be derived from the Hagen−Poiseuille law[40]

$$k_f = w^2/12 \quad (2)$$

with w being the mean hydraulic fracture width or aperture. Because of the concept of laminar flow, the total volumetric flow rate is the sum of the fracture flow and the matrix flow rate. The pressure drop in the matrix and fracture is assumed to be the same, so that

$$k_f = \frac{k_{av}A - k_m(A - wL)}{wL} \quad (3)$$

with k_{av}, k_m, and k_f being the average, matrix, and fracture permeability, respectively. A and L are the cross-sectional area (m^2) and the sample's length (m), and w is the hydraulic fracture aperture (m). The INT-plug was used to obtain an indication of the matrix permeability at different confining pressures. This method provides an average aperture for an idealized fracture, which must be considered as an equivalent aperture through which fluid flow takes place.[41,42]

Local Aperture Quantification. On the basis of the micro-CT images, local fracture apertures can be quantified to assess the aperture distribution. The Acquila software (XRE NV, Belgium) was used to reconstruct the micro-CT scans, while Avizo (FEI) was used to analyze the reconstructed images in 3D. The XLab-Simulation extension within Avizo allows one to calculate absolute permeabilities and local fluid velocities. In this study, this was used to calculate the fracture permeability in the IF-plug at different confining pressures, on the basis of the segmented fracture. Local fracture apertures were determined on the differential images:[24,43] gray value profiles were taken perpendicular to the fracture orientation so that the fracture's gray value dip could be fitted by a Gaussian point-spread function (PSF).[25,44,45] In case of well pronounced fractures, as in the IF-plug, the full-width-half-maximum (fwhm) of the PSF dip is an appropriate method to determine local apertures.[25,46] For each scan of the IF-plug, a total of 1200 gray value profiles were analyzed. Each fit was visually evaluated for its accuracy and discarded when considered insufficient. To obtain a second evaluation of the measurements, they were taken along three vertical scanlines, which implies that the measurements along a single scanline had a spacing equal to the resolution of the micro-CT images. Measurements along such a scanline thus need to show a logical progression from one measurement to the other. Because of the amount of measurements, we believe the fracture's aperture has been sampled in a representative manner. To improve the representativeness, one could obtain aperture measurements based on a 2D grid overlying the fracture. We attempted to extract gray value profiles that were perpendicular to the fracture. Deviations from perpendicularity result in slightly overestimated apertures; however, local fracture apertures were quantified at identical locations in the rock plug at different confining pressures due to the image registration. Therefore, the measured data gives a good representation of the fracture closure at different confining pressures.

In the NF-plug, the fracture is known to be thinner. In such fractures, the missing attenuation (MA) can be determined in the gray value dip described by the PSF.[25,46] The aperture distribution of the NF-plug was determined on gray value profiles in the dry scans and thus not on differential images. Figure S4 illustrates the difference between the MA measurement of an attenuation dip and the fwhm determination of the fractures' aperture. The general equation describing the MA method can be found in the Supporting Information, together with an illustration describing the different parameters for its calculation (Figure S5).

RESULTS AND DISCUSSION

Micro-CT Results. Figure 1 illustrates the obtained micro-CT data of the IF-plug at a confining pressure of 2 MPa. The

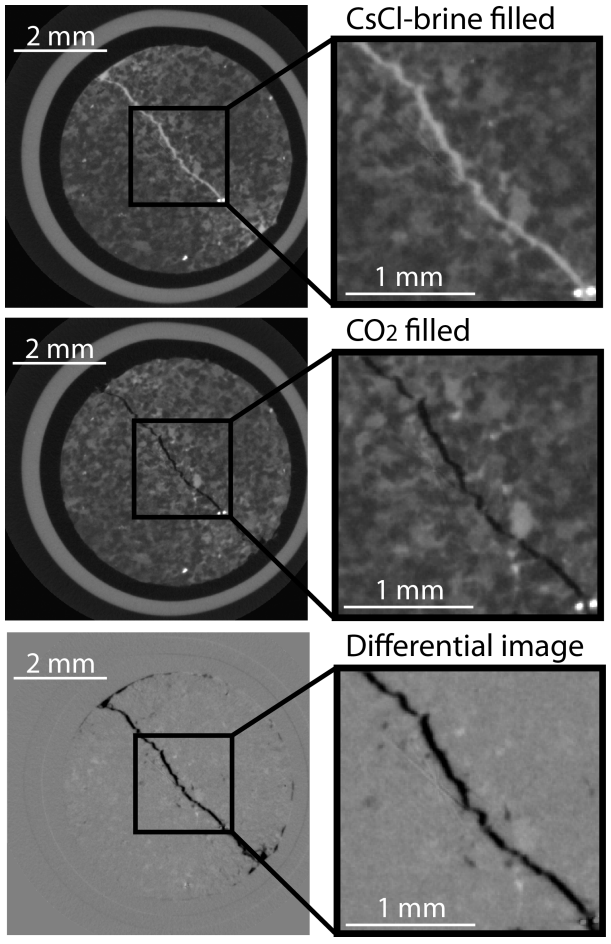

Figure 1. Micro-CT images of the IF-plug are depicted at a confining pressure of 2 MPa. The registration of the CsCl-brine filled state and the dry state allow differential images to be constructed. The insets show the results more clearly for the three cases.

images in which the sample is filled with CsCl-brine (Figure 1, top) are registered with those in which the fracture was drained by CO_2 (Figure 1, middle) in order to construct the differential image (Figure 1, bottom). This allowed the segmentation and quantification of the fracture in the IF-plug, even at higher confining pressures. However, because of the experimental approach used with the NF-plug, differential images between

DOI: 10.1021/acs.est.8b00861
Environ. Sci. Technol. 2018, 52, 4546−4554

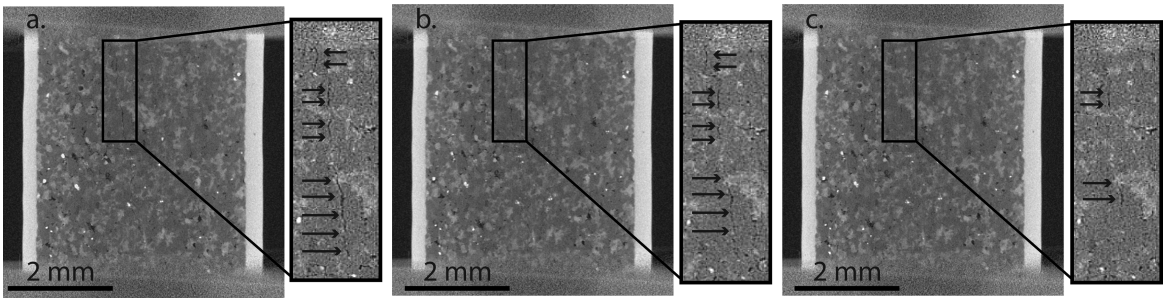

Figure 2. Vertical cross-sections through the micro-CT data of the NF-plug: (a) at a confining pressure of 2.9 MPa; (b) at a confining pressure of 5.0 MPa; (c) at a confining pressure of 10.0 MPa. The gradual closure of the fracture is emphasized in the insets, in which the image is adjusted to enhance sharpness and contrast and the fracture is highlighted with arrows.

the dry state of the sample and a CsCl-brine filled state did not fully represent the entire fracture: the fracture remained partially closed after the sample was brought to a confining pressure of 15 MPa in a dry state and subsequently brought back to atmospheric conditions. Therefore, in the second NF-plug experiment, with the CsCl-brine, the fracture does not have the same aperture distribution anymore. Aperture measurements in the NF-plug therefore remain limited to areas in which the fracture is well-pronounced in the first set of scans (in the dry state). The results of these scans are shown in Figure 2. In this plug, the fracture aperture distribution is close to the image resolution (11 μm), making it challenging to quantify it at different locations within the plug.

Permeability Changes. The permeability measurements of the three plugs at different confining pressures are summarized in Figure 3. The permeability of the INT-plug (Figure 3A) shows an exponential decrease with increasing confinement. The data can be fitted with an exponential function with exponent −0.254 (R^2 value of 0.99). Where previous measurements of unfractured rock cores from the Longyearbyen CO_2 project showed a linear permeability decrease with increasing confining pressure,[16] the exponential behavior could indicate the presence of fractures below the spatial resolution of the images. At a confining pressure of 5 MPa, the tested rock plug exhibits a permeability decrease of up to 64% compared to a confinement of 1 MPa (0.43×10^{-17} m^2 versus 1.2×10^{-17} m^2).

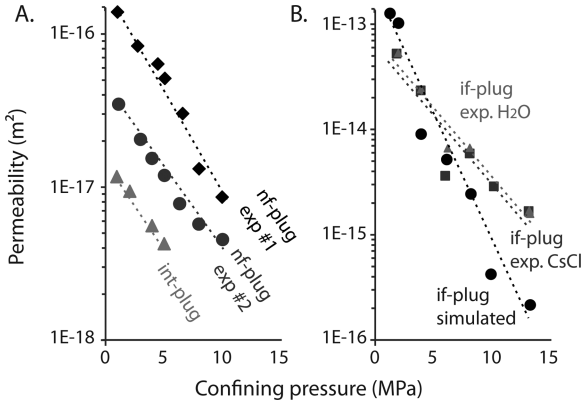

Figure 3. Permeability measurements and simulations based on the X-ray micro-CT images, as a function of the applied confining pressure. (A) Permeability of the INT-plug (triangles), compared to the NF-plug (squares and circles), in which the permeability was determined in two consecutive runs. (B) Experimental permeability of the IF-plug, in which the permeability was determined both with a CsCl-brine and H_2O, and the simulated permeability, based on the segmentation of the fracture from the micro-CT images.

For the IF-plug, the permeability in function of the confinement is shown in Figure 3b. Permeability was measured both with H_2O and the CsCl-brine, by changing the pore fluid at each of the confining pressures (Figure S3). Measurements with both pore fluids give very similar results. The permeability data obtained by flushing H_2O through the sample could be fitted by an exponential function with an exponent of −0.291 (R^2 value of 0.96). For the measurements in which the CsCl-brine was used, a fit with an exponent of −0.293 (R^2 value of 0.84) was obtained. The quality of the fits was affected by outlying values for the permeability at a confining pressure of 6.2 MPa.

The differential images between the CsCl-brine-filled state and the state with the drained fracture were used as a basis for fracture segmentation and fluid flow simulations with the Avizo extension XLab-Simulation. This software package solves the Stokes equations and calculates the absolute permeability tensor through the Darcy equation. No-slip boundary conditions were used, and permeability was only determined parallel to the fracture, which is equal to the experimental determination. A small subsection of the micro-CT images was used for these simulations, composed of 260 × 260 × 400 voxels. This was done to avoid edge effects within the small plug. In the differential images, the fracture was segmented on the basis of its gray value. For each of the confining pressures, the same gray value threshold was used. The simulations were carried out on the resulting segmented volume images. It is important to note that only the fracture was segmented from the images, so that the permeability results of the simulations, which are depicted in Figure 3b, are considered as the fracture permeability. They resemble the experimental total permeabilities quite well, especially at lower confining pressures. The edge effect is present in the experiments, but not in the simulations, and becomes more important at higher confining pressures. Overall, the total permeability nearly equals the fracture permeability in these experiments, because matrix permeability, measured in the INT-plug, is so small it can be neglected. However, since the permeability simulations are only carried out on the segmented fracture, we can expect discrepancies from the experimentally determined permeability. Taking the matrix permeability into consideration, and thus simulating flow through the entire rock plug, would increase the accuracy of the fluid flow simulations.[47] The flow simulations further allow one to visualize the local fluid velocities inside of the fracture (Figure 4). These results indicate the stepwise closure of the fracture, thereby cutting off part of the original

DOI: 10.1021/acs.est.8b00861
Environ. Sci. Technol. 2018, 52, 4546−4554

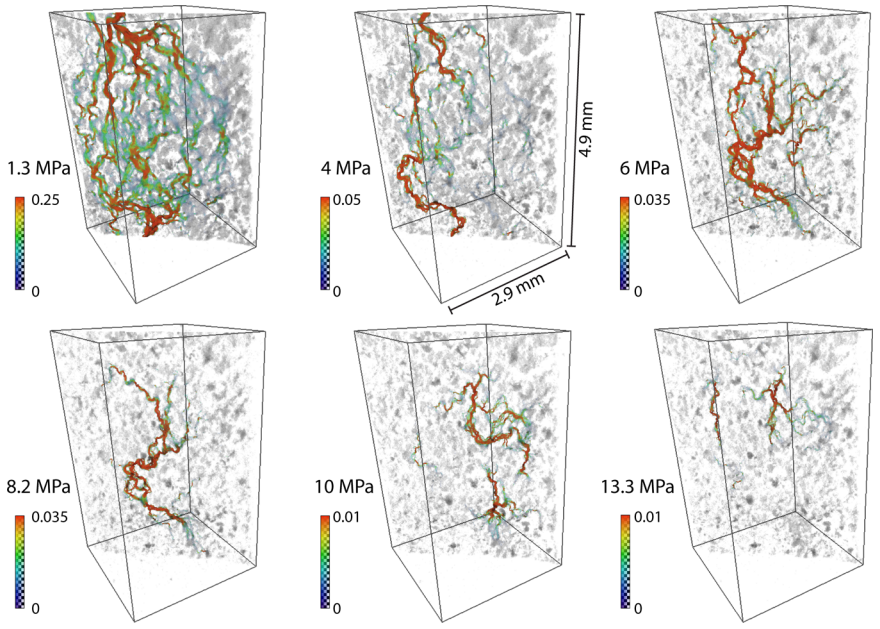

Figure 4. Visualization of fluid flow simulations in the IF-plugs, with increasing confining pressures. The simulations were carried out for identical regions within the rock plug, simulating a flow parallel to the fracture by solving the Stokes equations. It is important to note the decrease in local fluid velocity (in μm/s) with increasing pressure, as well as the channelization of the flow due to fracture closure.

Table 1. Fracture Width Determinations, Based on the Hagen−Poiseuille Law, Both for the Experimental Permeability Determination and the Simulated Permeability

confining pressure (MPa)	experimental permeability k_{av} (m^2)	extrapolated matrix permeability k_m (m^2)	average fracture width w (μm)	simulated fracture permeability k_f (m^2)	average fracture width w based on simulation (μm)
Sample with Induced Vertical Fracture					
2.0	5.3×10^{-14}	9.4×10^{-18}	9.6	1.0×10^{-13}	1.1
4.0	2.4×10^{-14}	5.6×10^{-18}	7.4	9.0×10^{-15}	0.3
6.2	5.1×10^{-15}	3.2×10^{-18}	4.4	5.2×10^{-15}	0.2
8.2	6.3×10^{-15}	1.9×10^{-18}	4.7	2.4×10^{-15}	0.2
10.2	2.9×10^{-15}	1.1×10^{-18}	3.6	4.2×10^{-16}	0.1
13.3	1.7×10^{-15}	0.5×10^{-18}	3.0	2.2×10^{-16}	0.1
Sample with Natural Vertical Fracture					
1.1	1.1×10^{-16}	1.2×10^{-17}	1.2		
2.9	5.2×10^{-17}	7.4×10^{-18}	0.9		
4.3	4.0×10^{-17}	5.2×10^{-18}	0.8		
5.1	3.2×10^{-17}	4.2×10^{-18}	0.8		
6.5	1.9×10^{-17}	3.0×10^{-18}	0.6		
8.0	9.4×10^{-18}	2.0×10^{-18}	0.5		
10.0	6.6×10^{-18}	1.2×10^{-18}	0.4		

fluid flow paths. At the lowest considered confinement (1.3 MPa), the simulations suggest channelized fluid flow, distributed throughout the entire fractured area. However, high local velocities are found at the inflow and outflow boundaries of the retained subvolume. This is due to local maxima in the fracture aperture at the boundaries of the retained volume, causing preferential in- and outflow at a certain location in the fracture. The fluid can then virtually spread out in the entire fracture, causing lower local fluid velocities in the central part of the fracture, after redirecting to the preferential outflow point. Much like in previous studies,[20,21] the increase in confining pressure causes preferential flow channels to form, which govern the principal fluid flow. The connectivity within the fracture and the local flow velocities are generally decreased. This is due to a decrease in average fracture aperture and the partial closure of the fracture.

The NF-plug was also tested for its permeability change under confinement (Figure 3a), both while saturated with CsCl-brine and H_2O, respectively. At the lowest confinement, the NF-plug exhibited a measured permeability approximately 20 times higher than the INT-plug. With increasing confining pressure, the permeability decreased exponentially, with a fitted exponent of −0.324 (R^2 value of 0.97). Compared to the IF-plug, the NF-plug is up to 1000 times less permeable; however, the exponential decrease is very similar. The micro-CT images have shown that the rock fracture remains partially closed after the initial increase in confining pressure. This was detected by comparing the micro-CT images of the second pressure cycle to the images of the initial cycle, as well as to micro-CT images from a third cycle, when the permeability experiment was run once more and even lower permeabilities were observed. The measurements from this third cycle, in which the experiment

DOI: 10.1021/acs.est.8b00861
Environ. Sci. Technol. 2018, 52, 4546−4554

was carried out with H_2O, could be fitted with an exponential function with exponent −0.237 (R^2 value of 0.98).

When comparing the exponents of the exponential fitting of the permeability data of the different rock plugs (Figure 3), all three plugs show similar behavior with increasing confining pressure. Although the data is too limited to extract a predictive model, it suggests that an induced fracture can be used to understand the fluid flow behavior of natural fractures in these sandstones. Moreover, it fits with the hypothesis that small, undetected microfractures are also present in the INT-plug.

Hydraulic Aperture Quantification. The permeability measurements and simulations further allow the determination of an average fracture aperture via eqs 2 and 3. In these equations, experimentally determined permeabilities represent the total permeability k_{av}, the permeability determined on the INT-plug represents the matrix permeability k_m, and the simulated permeabilities can be considered as fracture permeabilities k_f. These results and the corresponding hydraulic fracture apertures, based on the parallel plate representation of fractures,[39,40] are summarized in Table 1. The obtained hydraulic fracture apertures, either based on the experimental data or directly via eq 2 from the fracture permeability simulations, are found in the order of 10 μm and smaller for the IF-plug and only up to 1.1 μm for the NF-plug. These values are within the range expected from previous studies.[48] To compare the hydraulic apertures based on the experiments to those from simulated permeability measurements, the volume on which both were carried out has to be considered: for the simulations, only one-third of the actual fracture was taken into consideration, due to limitations in the imaging process.

During the experiments, maximum Reynold's numbers of 8.5×10^{-3} and 3.4×10^{-5} were obtained for the IF-plug and NF-plug, respectively. This is well within the laminar flow regime for fractures,[49] indicating the results of the simulations and the assumptions in eqs 2 and 3 to be valid. Although out of the scope of this work, the results depicted in Table 1, in combination with a field study on the concentration and connectivity of fractures,[13] lend themselves to the definition of large-scaled fractured rock permeability models.[50,51] Still, it remains important to understand the local variation in fracture aperture for a full understanding of the fluid flow behavior in the fractures and by extent in naturally fractured reservoirs.[42,52]

Local Aperture Quantification. At 7 different confining pressures, micro-CT scans of the IF-plug were made with the CsCl-brine as contrasting agent and a drained fracture due to injection of CO_2. The fracture aperture distribution was subsequently determined as fwhm values on the differential images of these scans.[24,43] At a confining pressure of 1 MPa, 765 out of the 1200 PSF fits were considered to be in agreement with the spread of the micro-CT data. However, at a confining pressure of 10 MPa, only 451 out of the 1200 PSF fits were accepted. This trend could be seen at the other confining pressures as well: the PSF fitting process is more successful for well-established fractures (at low confining pressure) as opposed to thin fractures (at higher confining pressure). Averaging these measurements might thus yield a biased fracture aperture distribution in the rock plug. Still, the measured apertures, presented in Figure 5, show the expected closure of the fracture with increasing confining pressure. Results from fwhm measurements taken at confining pressures of 8.2 and 13.3 MPa are not included in this figure. In these scans, the injection of CO_2 led to the local increase in brine concentration along the fracture. Due to the high solubility of

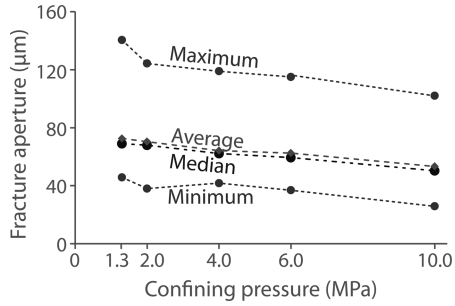

Figure 5. Minimum, maximum, average, and median fracture aperture, determined as fwhm values in the IF-plug as a function of applied confining pressure. The fwhm determination is capable of capturing the closure of the fracture with increasing confining pressure.

CsCl in water, the increase in brine concentration did not lead to salt precipitation, which could distort the permeability measurements. However, it led to a higher fwhm measurement which could not be compared to those at the other confining pressures. However, for the measurements at the retained confining pressures, the minimum, maximum, and median fracture width show a consistent decrease with increasing confining pressure (Figure 5). In the micro-CT slices where a fwhm could be determined both for a confining pressure of 1 and 10 MPa, the fracture closure can quantitatively be determined. In order to compare the fracture aperture measurements, all micro-CT scans were first registered to the scan taken at the lowest confining pressure. The aperture measurements were thus carried out at identical positions within each micro-CT scan. The incremental fracture closure at a given confining pressure can be found in Figure 5. It is important to note that the change in average and median aperture with increasing confining pressure must be considered as a minimum average change, since a fwhm value cannot be determined when the fracture is several times smaller than the image resolution. The observations are thus limited by the spatial resolution of the micro-CT scans, which makes a threshold for full fracture closure ambiguous.

Because the fracture in the NF-plug is very thin, the apertures can be determined with the MA method,[25,46] rather than with fwhm. However, the matrix heterogeneity of the rock complicates this quantification: as quartz and dolomite attenuate X-rays differently, they result in different gray values in the micro-CT images. Because the fracture tends to follow grain boundaries, it is often bound by the lighter gray dolomite on one side and the darker quartz on the other side. The MA determination of the fracture aperture is very susceptible to such a gradient across the fracture.[25] Therefore, MA measurements were restricted to small subsections along the fracture, where it was bounded by quartz grains at both sides. We assume that the local aperture distribution is independent from the bounding minerals and that this is thus a valid approach. Short gray value profiles along the fracture, which are the basis for the MA measurements, allow the determination of a local value for the average material CT value CT_{Mat} (Figure S5). This method allows for an aperture characterization at the edge of the resolution and below that. To illustrate this on the NF-plug, gray value profiles were made at confining pressures of 2.9, 5.0, and 10.0 MPa, across the lower section of the fracture shown in the vertical slices illustrated in Figure 2. The results of this MA determination are listed in Table 2. Only those measurements where a MA could be determined for at least two of the

DOI: 10.1021/acs.est.8b00861
Environ. Sci. Technol. 2018, 52, 4546−4554

Table 2. Fracture Aperture Based on the MA Method in the Naturally Fractured Rock Plug

aperture at conf. pressure of 2.9 MPa (μm)	aperture at conf. pressure of 5.0 MPa (μm)	aperture at conf. pressure of 10.0 MPa (μm)
14.8	8.2	4.3
7.3	5.4	5.0
9.8	4.8	
6.6	3.9	
3.6	4.3	4.7
8.9	3.6	
5.9	3.6	
	15.3	4.5
11.0	10.8	8.6
13.9	9.7	
22.2	8.1	
16.6	16.6	

confining pressures are included, resulting in 12 individual measurements which can be represented out of 30 measurements which were carried out. Ketcham et al.[25] have shown that these measurements are reliable down to one-tenth of a voxel width. In this case, it corresponds to measurements as small as 1.1 μm. Because of the difficulty in fracture segmentation, it was impossible to carry out these measurements in an automatic way to perform statistical analysis on them. Much like the fwhm measurements in the IF-plug, however, the MA measurements show a logical decrease of the fracture width with increasing confining pressure. We therefore assume that the MA measurements provide reliable approximations of the local fracture width.

When comparing the local apertures, determined by the fwhm and the MA method, to the hydraulic apertures, we see that the measured local apertures are distinctively larger than the corresponding hydraulic apertures at the same confining pressure. This is explained by the differences in observation: the hydraulic apertures represent ideal fractures (parallel fracture walls) with the same permeability as the rough fractures. Since the natural and induced fractures are rough, they can fully close at certain fracture locations. As such, fluid flow does not take place in the entire fracture. Therefore, the local apertures can be several times larger than the hydraulic aperture. The fact that even the minimum values of the measured local apertures (Figure 5) are larger than the hydraulic apertures at the same confining pressures (Table 1) is linked to the limitation of determining a PSF on the micro-CT data. The smaller the fracture, the more difficult it is to fit the data with a correct PSF. However, on the basis of the permeability data represented in Figure 3 and the fluid flow simulations in Figure 4, it is safe to assume that the distribution and closure of these small apertures along the fracture play an important role in inhibiting the fluid flow and thus lowering the local permeability of the rock plugs.

Environmental Implications. On Svalbard, an unconventional CO_2 storage unit is targeted which relies heavily on fracture permeability for its total hydraulic conductivity and, to a lesser extent, storage capacity. In this study, permeability measurements indicate a partial closure of rock fractures with increasing confining pressure, which can be confirmed by local fracture aperture measurements and fluid flow simulations based on the extraction of the 3D fracture volume in micro-CT images at different confining pressures. Although they partially close, fractures still provide the main fluid pathways at greater depths. At a confining pressure of 10 MPa (equal to a burial depth of approximately 900 m), rock plugs with natural and induced fractures are characterized by a permeability of approximately five times and more than a thousand times the permeability of an unfractured sample at the same conditions, respectively. At this depth, the natural and induced fractures are characterized by hydraulic apertures in the order of 1 and 10 μm, respectively. Even such small fractures will thus influence the overall injectivity and storage capacity of the reservoir. The role of natural fractures in this system can be studied through fractures induced by a tensile splitting test, which show very similar behavior. In this setting, the induced fractures, which allow for a better visualization and quantification of the fracture apertures based on the micro-CT images, can be used to determine the relative closure of the fracture with increasing depths. As such, natural fractures can be investigated within decompacted core samples or in outcrop material after which a certain amount of closure can be inferred from measurements in induced fractures. In this particular case, both natural and induced fractures closed under the influence of increased confining pressure on the rock plugs, with apertures closing to approximately 40% of their original size as the confining pressure increased from 1 to 10 MPa. This coincides with a permeability drop of more than 90%. Although upscaling to the continuum scale is a difficult task, information on the fracture behavior at depth is necessary for reservoir modeling. In this work, we presented a methodology to obtain this information from either direct aperture measurements or, in an indirect way, via the hydraulic aperture determination. The rock plugs in this study strongly rely on the fractures for their fluid conductivity. However, they are fairly homogeneous at the scale of observation and lack the presence of clays which could have an important impact on fracture closure. These are definitely factors one would have to take into account when developing reservoir models based on the experiments described in this work. Although this study focused on a specific, small scale CO_2 project, it helps in the understanding of fractured unconventional reservoirs elsewhere and low-permeability cap rocks. Advanced micro-CT imaging of in situ triaxial rock tests has been proven to allow one to investigate the controlling factors for pore-scale transport through such reservoir material targeted for CO_2 sequestration.

■ ASSOCIATED CONTENT

Supporting Information

The Supporting Information is available free of charge on the ACS Publications website at DOI: 10.1021/acs.est.8b00861.

Additional information on the fracture drainage process; calibration techniques for the micro-CT images and the fwhm and MA method; general equation for the MA determination; geological overview of the targeted CO_2 injection area (Figure S1); schematic representation of the experimental setup (Figure S2); schematic representation of the experimental approach for the IF- and NF-plug (Figure S3); illustration of the difference between the fwhm and the MA method (Figure S4); example of a PSF fit to CT data with indication of parameters for the determination of the MA (Figure S5); scanning parameters for the micro-CT imaging (Table T1) (PDF)

DOI: 10.1021/acs.est.8b00861
Environ. Sci. Technol. 2018, 52, 4546−4554

AUTHOR INFORMATION

Corresponding Author

*E-mail: Jeroen.VanStappen@UGent.be or j.f.vanstappen@uu.nl.

ORCID

Jeroen F. Van Stappen: 0000-0003-2191-2888

Tim De Kock: 0000-0001-5096-1473

Present Addresses

[†]J.F.V.S.: High Pressure and Temperature Laboratory, Department of Earth Sciences, Faculty of Geosciences, Utrecht University, P.O. Box 80.021, 3508TA Utrecht, The Netherlands.

[ϕ]T.B.: Department of Earth Science and Engineering, Imperial College London, South Kensington Campus, SW7 2AZ, London, United Kingdom.

Author Contributions

The manuscript was written through contributions of all authors. All authors have given approval to the final version of the manuscript.

Notes

The authors declare no competing financial interest.

ACKNOWLEDGMENTS

The authors would like to acknowledge SINTEF, Norway, for providing the in situ triaxial device, allowing the experiments to be performed at the Centre for X-ray Tomography at Ghent University, Belgium. The experimental rock deformation/HPT-lab at Utrecht University, The Netherlands, is acknowledged for the help in controlling the triaxial device. The Special Research Fund (BOF) at Ghent University is acknowledged for the finalizing PhD grant 01DI1316 for J.F.V.S. Also, the Research Foundation−Flanders (FWO) is acknowledged for funding the project 3G024212. T.D.K. is a postdoctoral fellow of the Research Foundation−Flanders and acknowledges its support. This study is part of the studies at the UNIS CO_2 LAB (http://co2-ccs.unis.no), an industry and Research Council of Norway (the Climit program) sponsored project. Dr. Suzanne Hangx is thanked for providing helpful comments on the manuscript.

ABBREVIATIONS

CCS	carbon dioxide capture and storage
CsCl	cesium chloride
EMCT	environmental micro-CT system
fwhm	full-width-half-maximum
IPCC	Intergovernmental Panel on Climate Change
MA	missing attenuation
micro-CT	high resolution X-ray computed tomography
PSF	point-spread function
UGCT	Centre for X-ray Tomography at Ghent University

REFERENCES

(1) Metz, B.; Davidson, O.; De Coninck, H.; Loos, M.; Meyer, L. *IPCC Special Report on Carbon Dioxide Capture and Storage*; Cambridge University Press: Cambridge, UK, 2005.

(2) Edenhofer, O., Pichs-Madruga, R., Sokona, Y., Farahani, E., Kadner, S., Seyboth, K., Adler, A., Baum, I., Brunner, S., Eickemeier, P., et al.., Eds. *Climate Change 2014: Mitigation of Climate Change, Contribution of Working Group III to the Fifth Assessment Report of the Intergovernmental Panel on Climate Change*; Cambridge University Press: Cambridge, United Kingdom and New York, NY, USA, 2014.

(3) Würdemann, H.; Möller, F.; Kühn, M.; Heidug, W.; Christensen, N. P.; Borm, G.; Schilling, F. R. The CO2SINK group. CO2SINK-From Site Characterisation and Risk Assessment to Monitoring and Verification: One Year of Operational Experience with the Field Laboratory for CO2 Storage at Ketzin, Germany. *Int. J. Greenhouse Gas Control* **2010**, *4* (6), 938−951.

(4) Doughty, C.; Freifeld, B. M.; Trautz, R. C. Site Characterization for CO2 Geologic Storage and Vice Versa: The Frio Brine Pilot, Texas, USA as a Case Study. *Environ. Geol.* **2008**, *54* (8), 1635−1656.

(5) Orr, F. M., Jr. CO2 Capture and Storage: Are We Ready? *Energy Environ. Sci.* **2009**, *2* (5), 449−458.

(6) Arts, R.; Chadwick, A.; Eiken, O.; Thibeau, S.; Nooner, S. Ten Years' Experience of Monitoring CO2 Injection in the Utsira Sand at Sleipner, Offshore Norway. *First Break* **2008**, *26* (1), 65−72.

(7) Benson, S.; Cook, P.; Anderson, J.; Bachu, S.; Nimir, H. B.; Basu, B.; Bradshaw, J.; Deguchi, G.; Gale, J.; von Goerne, G.; et al. Underground Geological Storage. In *IPCC special report on carbon dioxide capture and storage*; Cambridge University Press: Cambridge, UK, 2005; pp 195−276.

(8) Braathen, A.; Bælum, K.; Christiansen, H. H.; Dahl, T.; Elvebakk, H.; Hansen, F.; Hanssen, T. H.; Jochmann, M.; Johansen, T. A.; Johnsen, H.; et al. The Longyearbyen CO2 Lab of Svalbard, Norway - Initial Assessment of the Geological Conditions for CO2 Sequestration. *Nor. J. Geol.* **2012**, *92*, 353−376.

(9) Senger, K.; Tveranger, J.; Braathen, A.; Olaussen, S.; Ogata, K.; Larsen, L. CO2 Storage Resource Estimates in Unconventional Reservoirs: Insights from a Pilot-Sized Storage Site in Svalbard, Arctic Norway. *Environ. Earth Sci.* **2015**, *73* (8), 3987−4009.

(10) UNIS CO2 Lab. *The Longyearbyen CO2 Lab Phase 2 Final Report*; UNIS: Longyearbyen, 2015.

(11) Mørk, M. B. E. Diagenesis and Quartz Cement Distribution of Low-Permeability Upper Triassic - Middle Jurassic Reservoir Sandstones, Longyearbyen CO2 Lab Well Site in Svalbard, Norway. *AAPG Bull.* **2013**, *97* (4), 577−596.

(12) Magnabosco, C.; Braathen, A.; Ogata, K. Permeability Model of Tight Reservoir Sandstones Combining Core-Plug and Miniperm Analysis of Drillcore; Longyearbyen CO2 Lab, Svablard. *Nor. J. Geol.* **2014**, *94*, 189−200.

(13) Ogata, K.; Senger, K.; Braathen, A.; Tveranger, J.; Olaussen, S. Fracture Systems and Mesoscale Structural Patterns in the Siliciclastic Mesozoic Reservoir-Caprock Succession of the Longyearbyen CO2 Lab Project: Implications for Geological CO2 Sequestration in Central Spitsbergen, Svalbard. *Nor. J. Geol.* **2014**, *94*, 121−154.

(14) Van Stappen, J.; De Kock, T.; Boone, M. A.; Olaussen, S.; Cnudde, V. Pore-Scale Characterisation and Modelling of CO2 Flow in Tight Sandstones Using X-Ray Micro-CT; Knorringfjellet Formation of the Longyearbyen CO2 Lab, Svalbard. *Nor. J. Geol.* **2014**, *94* (2−3), 201−215.

(15) Sahimi, M. Characterization of Fractures, Fracture Networks and Fractured Porous Media. In *Flow and transport in Porous media and fractured rock: from classical methods to modern approaches*; Wiley: New York, 2011; pp 143−177.

(16) Farokhpoor, R.; Baghbanbashi, T.; Torsæter, O.; Lindeberg, E.; Mørk, A. Experimental and Simulation Analysis of CO2 Storage in Tight and Fractured Sandstone under Different Stress Conditions. In *73rd European Association of Geoscientists and Engineers Conference and Exhibition 2011: Unconventional Resources and the Role of Technology. Incorporating SPE EUROPEC*, Vienna, Austria, May 23−26, 2011; SPE-143589-MS; Vol. *1*, p 1−10.

(17) Watanabe, N.; Ishibashi, T.; Ohsaki, Y.; Tsuchiya, Y.; Tamagawa, T.; Hirano, N.; Okabe, H.; Tsuchiya, N. X-Ray CT Based Numerical Analysis of Fracture Flow for Core Samples under Various Confining Pressures. *Eng. Geol.* **2011**, *123*, 338−346.

(18) Deng, H.; Fitts, J. P.; Crandall, D.; Mcintyre, D.; Peters, C. A. Alterations of Fractures in Carbonate Rocks by CO2 Acidified Brines. *Environ. Sci. Technol.* **2015**, *49*, 10226−10234.

(19) Cai, Y.; Liu, D.; Mathews, J. P.; Pan, Z.; Elsworth, D.; Yao, Y.; Li, J.; Guo, X. Permeability Evolution in Fractured Coal — Combining Triaxial Confinement with X-Ray Computed Tomography, Acoustic Emission and Ultrasonic Techniques. *Int. J. Coal Geol.* **2014**, *122*, 91−104.

DOI: 10.1021/acs.est.8b00861
Environ. Sci. Technol. 2018, 52, 4546−4554

(20) Kling, T.; Huo, D.; Schwarz, J.-O.; Enzmann, F.; Benson, S.; Blum, P. Simulating Stress-Dependent Fluid Flow in a Fractured Core Sample Using Real-Time X-Ray CT Data. *Solid Earth* **2016**, *7* (4), 1109−1124.
(21) Huo, D.; Benson, S. M. An Experimental Investigation of Stress-Dependent Permeability and Permeability Hysteresis Behavior in Rock Fractures. In *Fluid dynamics in complex fractured-porous systems*; Faybishenko, B., Benson, S. M., Gale, J. E., Eds.; John Wiley & Sons, Inc.: Hoboken, NJ, 2015; pp 99−114.
(22) Voorn, M.; Exner, U.; Rath, A. Multiscale Hessian Fracture Filtering for the Enhancement and Segmentation of Narrow Fractures in 3D Image Data. *Comput. Geosci.* **2013**, *57*, 44−53.
(23) Deng, H.; Fitts, J. P.; Peters, C. A. Quantifying Fracture Geometry with X-Ray Tomography: Technique of Iterative Local Thresholding (TILT) for 3D Image Segmentation. *Comput. Geosci.* **2016**, *20* (1), 231−244.
(24) Boone, M. A.; De Kock, T.; Bultreys, T.; De Schutter, G.; Vontobel, P.; Van Hoorebeke, L.; Cnudde, V. 3D Mapping of Water in Oolithic Limestone at Atmospheric and Vacuum Saturation Using X-Ray Micro-CT Differential Imaging. *Mater. Charact.* **2014**, *97*, 150−160.
(25) Ketcham, R. A.; Slottke, D. T.; Sharp, J. M. Three-Dimensional Measurement of Fractures in Heterogeneous Materials Using High-Resolution X-Ray Computed Tomography. *Geosphere* **2010**, *6* (5), 499−514.
(26) Huo, D.; Pini, R.; Benson, S. M. A Calibration-Free Approach for Measuring Fracture Aperture Distributions Using X-Ray Computed Tomography. *Geosphere* **2016**, *12*, 558−571.
(27) De Kock, T.; Boone, M. A.; De Schryver, T.; Van Stappen, J.; Derluyn, H.; Masschaele, B.; De Schutter, G.; Cnudde, V. A Pore-Scale Study of Fracture Dynamics in Rock Using X-Ray Micro-CT under Ambient Freeze-Thaw Cycling. *Environ. Sci. Technol.* **2015**, *49* (5), 2867−2874.
(28) Cnudde, V.; Boone, M. N. High-Resolution X-Ray Computed Tomography in Geosciences: A Review of the Current Technology and Applications. *Earth-Sci. Rev.* **2013**, *123*, 1−17.
(29) Bultreys, T.; Boone, M. A.; Boone, M. N.; De Schryver, T.; Masschaele, B.; Van Hoorebeke, L.; Cnudde, V. Fast Laboratory-Based Micro-Computed Tomography for Pore-Scale Research: Illustrative Experiments and Perspectives on the Future. *Adv. Water Resour.* **2016**, *95*, 341−351.
(30) Wildenschild, D.; Sheppard, A. P. X-Ray Imaging and Analysis Techniques for Quantifying Pore-Scale Structure and Processes in Subsurface Porous Medium Systems. *Adv. Water Resour.* **2013**, *51*, 217−246.
(31) Andrew, M.; Bijeljic, B.; Blunt, M. J. New Frontiers in Experimental Geoscience: X-Ray Microcomputed Tomography and Fluid Flow. *Microsc. Anal.* **2014**, *130*, s4−s7.
(32) Deng, H.; Voltolini, M.; Molins, S.; Steefel, C. I.; DePaolo, D. J.; Ajo-Franklin, J.; Yang, L. Alteration and Erosion of Rock Matrix Bordering a Carbonate-Rich Shale Fracture. *Environ. Sci. Technol.* **2017**, *51* (15), 8861−8868.
(33) Harland, W. B.; Geddes, I. Chapter 18: Triassic History. In *The Geology of Svalbard*; Harland, B., Ed.; The Geological Society: London, 1997; pp 340−362.
(34) Tharp, T. M. Conditions for Crack Propagation by Frost Wedging. *Geol. Soc. Am. Bull.* **1987**, *99* (1), 94−102.
(35) Kwak, H. T.; Zhang, G.; Songhua, C. The Effects of Salt Type and Salinity on Formation Water Viscosity and NMR Responses. In *Proceedings of the Society of Core Analysts*, Toronto, Canada, August 21−25, 2005; SCA2005-51; p 1−13.
(36) Dierick, M.; Van Loo, D.; Masschaele, B.; Van den Bulcke, J.; Van Acker, J.; Cnudde, V.; Van Hoorebeke, L. Recent Micro-CT Scanner Developments at UGCT. *Nucl. Instrum. Methods Phys. Res., Sect. B* **2014**, *324*, 35−40.
(37) Masschaele, B. C.; Cnudde, V.; Dierick, M.; Jacobs, P.; Van Hoorebeke, L.; Vlassenbroeck, J. UGCT: New X-Ray Radiography and Tomography Facility. *Nucl. Instrum. Methods Phys. Res., Sect. A* **2007**, *580* (1), 266−269.
(38) Zimmerman, R. W.; Al-Yaarubi, A.; Pain, C. C.; Grattoni, C. A. Non-Linear Regimes of Fluid Flow in Rock Fractures. *Int. J. Rock Mech. Min. Sci.* **2004**, *41*, 163−169.
(39) Snow, D. T. Rock Fracture Spacings, Openings, and Porosities. *J. Soil Mech. Found. Div.* **1968**, *94* (1), 73−91.
(40) Witherspoon, P. A.; Wang, J. S. Y.; Iwai, K.; Gale, J. E. Validity of Cubic Law for Fluid Flow in a Deformable Rock Fracture. *Water Resour. Res.* **1980**, *16* (6), 1016−1024.
(41) Hakami, E.; Larsson, E. Aperture Measurements and Flow Experiments on a Single Natural Fracture. *Int. J. Rock Mech. Min. Sci. Geomech. Abstr.* **1996**, *33* (4), 395−404.
(42) Nick, H.; Paluszny, A.; Blunt, M. J.; Matthai, S. Role of Geomechanically Grown Fractures on Dispersive Transport in Heterogeneous Geological Formations. *Phys. Rev. E. Stat. Nonlin. Soft Matter Phys.* **2011**, *84* (5Pt 2), 1−9.
(43) Ketcham, R. A.; Iturrino, G. J. Nondestructive High-Resolution Visualization and Measurement of Anisotropic Effective Porosity in Complex Lithologies Using High-Resolution X-Ray Computed Tomography. *J. Hydrol.* **2005**, *302* (1−4), 92−106.
(44) Mazumder, S.; Wolf, K.-H. A. A.; Elewaut, K.; Ephraim, R. Application of X-Ray Computed Tomography for Analyzing Cleat Spacing and Cleat Aperture in Coal Samples. *Int. J. Coal Geol.* **2006**, *68* (3), 205−222.
(45) Vandersteen, K.; Busselen, B.; Van Den Abeele, K.; Carmeliet, J. Applications of X-Ray Computed Tomography in the Geosciences. In *Geological Society, London, Special Publications*; Mees, F., Swennen, R., Van Geet, M., Jacobs, P., Eds.; Geological Society of London: London, 2003; Vol. *215*.
(46) Van Geet, M.; Swennen, R. Quantitative 3D-Fracture Analysis by Means of Microfocus X-Ray Computed Tomography (μCT): An Example from Coal. *Geophys. Res. Lett.* **2001**, *28*, 3333−3336.
(47) Hardebol, N. J.; Maier, C.; Nick, H.; Geiger, S.; Bertotti, G.; Boro, H. Multiscale Fracture Network Characterization and Impact on Flow: A Case Study on the Latemar Carbonate Platform. *J. Geophys. Res. Solid Earth* **2015**, *120* (12), 8197−8222.
(48) Farokhpoor, R.; Torsaeter, O.; Baghbanbashi, T.; Mørk, A.; Lindeberg, E. Experimental and Numerical Simulation of CO2 Injection Into Upper-Triassic Sandstones in Svalbard, Norway. In *SPE International Conference on CO2 Capture, Storage, and Utilization*, New Orleans, Louisiana, USA, November 10−12, 2010; SPE 139524; p 1−11.
(49) Mourzenko, V. V.; Thovert, J.-F.; Adler, P. M. Permeability of a Single Fracture; Validity of the Reynolds Equation. *J. Phys. II* **1995**, *5*, 465−482.
(50) Bisdom, K.; Nick, H. M.; Bertotti, G. An Integrated Workflow for Stress and Flow Modelling Using Outcrop-Derived Discrete Fracture Networks. *Comput. Geosci.* **2017**, *103*, 21−35.
(51) Salimzadeh, S.; Nick, H. M.; Zimmerman, R. W. Thermoporoelastic Effects during Heat Extraction from Low-Permeability Reservoirs. *Energy* **2018**, *142*, 546−558.
(52) Bisdom, K.; Bertotti, G.; Nick, H. M. The Impact of in-Situ Stress and Outcrop-Based Fracture Geometry on Hydraulic Aperture and Upscaled Permeability in Fractured Reservoirs. *Tectonophysics* **2016**, *690* (A), 63−75.

DOI: 10.1021/acs.est.8b00861
Environ. Sci. Technol. 2018, 52, 4546−4554